



ELSEVIER

Contents lists available at ScienceDirect

Nuclear Instruments and Methods in Physics Research A

journal homepage: www.elsevier.com/locate/nima

Detector for measuring the $\pi^+ \rightarrow e^+ \nu_e$ branching fraction



A.A. Aguilar-Arevalo^a, M. Aoki^b, M. Blecher^c, D. vom Bruch^{e,1}, D. Bryman^e, J. Comfortⁱ, S. Cuen-Rochin^e, L. Doria^{d,*}, P. Gumplinger^d, A. Hussein^f, Y. Igarashi^g, N. Ito^b, S. Ito^b, S.H. Kettell^h, L. Kurchaninov^d, L. Littenberg^h, C. Malbrunot^{e,*,2}, R.E. Mischke^d, A. Muroi^b, T. Numao^d, G. Sheffer^d, A. Sher^{d,*,3}, T. Sullivan^e, K. Tauchi^g, D. Vavilov^d, K. Yamada^{b,3}, M. Yoshida^{b,4}

^a Instituto de Ciencias Nucleares, Universidad Nacional Autónoma de México, D.F. 04510 México, Mexico

^b Graduate School of Science, Osaka University, Toyonaka, Osaka 560-0043, Japan

^c Virginia Polytechnic Institute and State University, Blacksburg, VA 24061, USA

^d TRIUMF, Vancouver, BC, Canada V6T 2A3

^e Department of Physics and Astronomy, University of British Columbia, Vancouver, BC, Canada V6T 1Z1

^f University of Northern British Columbia, Prince George, BC, Canada V2N 4Z9

^g KEK, Tsukuba-shi, Ibaragi, Japan

^h Brookhaven National Laboratory, Upton, NY 11973-5000, USA

ⁱ Arizona State University, Tempe, AZ 85287-1504, USA

ARTICLE INFO

Article history:

Received 9 January 2015

Received in revised form

31 March 2015

Accepted 4 April 2015

Available online 13 April 2015

Keywords:

Nal(Tl)

CsI

Scintillation detectors

Pion decay

ABSTRACT

The PIENU experiment at TRIUMF is aimed at a measurement of the branching ratio $R^{e/\mu} = \Gamma(\pi^+ \rightarrow e^+ \nu_e) + (\pi^+ \rightarrow e^+ \nu_e \gamma) / \Gamma(\pi^+ \rightarrow \mu^+ \nu_\mu) + (\pi^+ \rightarrow \mu^+ \nu_\mu \gamma)$ with precision $< 0.1\%$. Incident pions, delivered at the rate of 60 kHz with momentum 75 MeV/c, were degraded and stopped in a plastic scintillator target. Pions and their decay product positrons were detected with plastic scintillators and tracked with multiwire proportional chambers and silicon strip detectors. The energies of the positrons were measured in a spectrometer consisting of a large Nal(Tl) crystal surrounded by an array of pure CsI crystals. This paper provides a description of the PIENU experimental apparatus and its performance in pursuit of $R^{e/\mu}$.

© 2015 Elsevier B.V. All rights reserved.

1. Introduction

Measurement of the branching ratio

$$R^{e/\mu} = \frac{\Gamma(\pi^+ \rightarrow e^+ \nu_e) + (\pi^+ \rightarrow e^+ \nu_e \gamma)}{\Gamma(\pi^+ \rightarrow \mu^+ \nu_\mu) + (\pi^+ \rightarrow \mu^+ \nu_\mu \gamma)}$$

compared to its precise Standard Model (SM) prediction provides a stringent test of the hypothesis of $e-\mu$ universality in weak interactions. The most recent experimental measurements of the

branching ratio are

$$R_{\text{TRIUMF}}^{e/\mu} = (1.2265 \pm 0.0034(\text{stat}) \pm 0.0044(\text{syst})) \times 10^{-4} [1, 2]$$

and

$$R_{\text{PSI}}^{e/\mu} = (1.2346 \pm 0.0035(\text{stat}) \pm 0.0036(\text{syst})) \times 10^{-4} [3].$$

These measurements are in agreement with the prediction:

$$R_{\text{SM}}^{e/\mu} = 1.2352(1) \times 10^{-4} [4, 5].$$

The order of magnitude gap in the precision of the experimental measurements and the theoretical prediction provides an opportunity to test the SM and to search for physics beyond it. Because of helicity-suppression of $\pi^+ \rightarrow e^+ \nu_e$ decay in the SM, helicity-suppressed contributions due to pseudoscalar or scalar couplings not present in the SM could result in a deviation of $R^{e/\mu}$ from the SM prediction. A measurement of $R^{e/\mu}$ with $< 0.1\%$ precision can probe new physics at mass scales up to 1000 TeV for pseudoscalar interactions [6].

The PIENU experimental technique is based on observing positrons from decays of pions at rest in an active plastic scintillator target. Muons from the dominant $\pi^+ \rightarrow \mu^+ \nu_\mu$ decay,

* Corresponding author.

** Primary corresponding author.

E-mail addresses: luca@triumf.ca (L. Doria), chloe.m@cern.ch (C. Malbrunot), sher@triumf.ca (A. Sher).

¹ Present address: Physikalisches Institut, Universität Heidelberg, Heidelberg, Germany.

² Present address: CERN, 1211 Geneva 21, Switzerland and Stefan-Meyer-Institut für subatomare Physik, Austrian Academy of Sciences, Boltzmanngasse 3, A-1090 Vienna, Austria.

³ Present address: Nagoya Koyo Senior High School, Japan.

⁴ Present address: KEK, 1-1 Oho, Tsukuba-shi, Ibaragi, Japan.

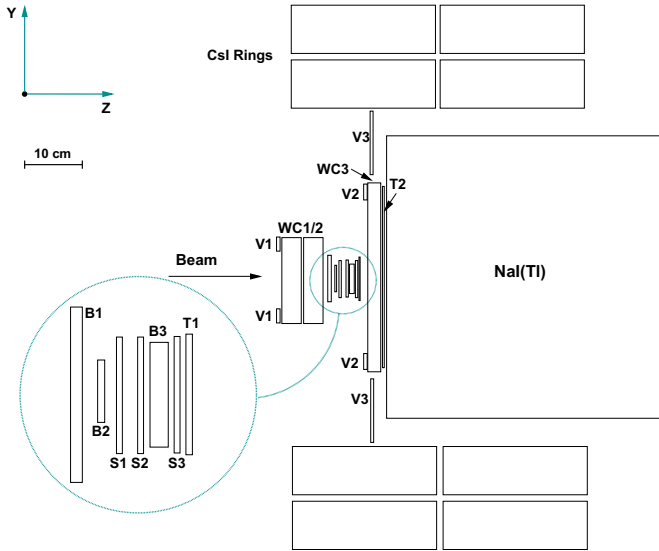


Fig. 1. Schematic diagram of the experimental apparatus. See text.

which have a kinetic energy of 4.1 MeV and a range of about 1 mm, were stopped in the target. By measuring the time and energy of positrons from the decays $\pi^+ \rightarrow e^+ \nu_e$ and $\mu^+ \rightarrow e^+ \nu_e \bar{\nu}_\mu$ following the decay $\pi^+ \rightarrow \mu^+ \nu_\mu$ ($\pi^+ \rightarrow \mu^+ \rightarrow e^+$ decay chain), $R^{e/\mu}$ can be obtained after applying several corrections. Since the positrons from the $\pi^+ \rightarrow e^+ \nu_e$ decay are monochromatic ($T_{\pi \rightarrow e \nu} = 69.3$ MeV), and positrons from the $\pi^+ \rightarrow \mu^+ \rightarrow e^+$ decay chain have a three-body decay energy spectrum with the highest positron kinetic energy cutoff at 52.3 MeV, the measured energy is used to separate the two decay modes. The raw branching ratio is extracted by performing a simultaneous fit of the time spectra of high energy ($T_e > 52$ MeV) and low energy ($T_e < 52$ MeV) samples to determine the yields of $\pi^+ \rightarrow e^+ \nu_e$ and $\pi^+ \rightarrow \mu^+ \rightarrow e^+$ decay chain events while taking backgrounds into account. Normalization factors, such as the solid angle of positron detection, cancel to first order, and the measured decay yields must be corrected for small energy-dependent effects, such as those from multiple Coulomb scattering, Bhabha scattering, and positron annihilation. For the final branching ratio determination additional corrections are applied including one which accounts for those $\pi^+ \rightarrow e^+ \nu_e$ decays excluded from the high energy time spectrum due to electromagnetic shower leakage and other effects. The latter correction and its systematic uncertainty were empirically determined from data and measurements of the response of the calorimetry system.

The PIENU detector had a solid angle acceptance⁵ for positrons emitted from the stopping target of 25%, which is eight times higher than the previous TRIUMF experiment [2]. In addition to measuring $R^{e/\mu}$, because of the increased acceptance and better energy resolution, the PIENU experiment was also able to perform a more sensitive search for heavy neutrinos in the $\pi^+ \rightarrow e^+ \nu_H$ decay [7].

2. Experimental overview

The TRIUMF cyclotron delivered a 500 MeV proton beam with an intensity of 120 μA to a 12 mm thick beryllium pion production target. A positively charged beam of momentum $P = 75$ MeV/c was

collected at 135° and transported in vacuum in the upgraded M13 channel⁶ [8] to the PIENU apparatus.

The PIENU apparatus, schematically shown in Fig. 1, was placed immediately downstream of the exit of the M13 beamline. The end of the vacuum pipe was covered with a 101.6 mm diameter, 72.6 μm -thick stainless steel window. To reduce the neutral background coming from the pion production target area and collimators in the beamline, a 24.8 cm-thick 2.57×2.29 m² (width \times height) steel wall with a hole (26.67 cm diameter) for the beam pipe to go through was installed upstream of the detector assembly (Fig. 2).

During normal data taking, the beam was composed of 84% π^+ , 14% μ^+ and 2% e^+ . It was imaged by a circular multiwire proportional chamber package (WC1 and WC2, containing three wire planes each). Following WC2, the beam was degraded by two plastic scintillator counters B1 and B2 (beam counters) used for measuring time and energy loss for particle identification. The beam counters were followed by two pairs of Si strip detectors (S1 and S2) with strips oriented along the X and Y axes.⁷ An 8 mm thick plastic scintillator target (B3) was sandwiched between S2 and another X–Y Si strip pair (S3). A circular multiwire proportional chamber WC3, containing three wire planes, was positioned downstream of S3 and sandwiched between two plastic scintillators, T1 and T2 (telescope counters).

Incoming pions stopped in the center (± 1 mm along the Z-axis) of B3, and then decayed at rest. A coincidence of signals from T1 and T2 was used to define the on-line positron acceptance. WC3 and S3 were used to reconstruct charged particle tracks and define the final acceptance off-line. The 15% solid-angle acceptance of the crystal spectrometer was defined by a radius cut ($r = 6$ cm) in the central plane of WC3, which was located 5.5 cm downstream⁸ of B3. Accepted decay products entered a large single crystal NaI(Tl) detector (48 cm long and 48 cm diameter) [9]. In order to absorb shower leakage from the NaI(Tl) crystal and to detect large angle photons from radiative $\pi^+ \rightarrow e^+ \nu_e \gamma$ decay, it was enveloped by four rings of pure Csl crystals [10]. The NaI(Tl) and Csl crystal array served as the calorimeter to measure the energy of the decay product positrons.

Three annular scintillators, which covered inactive material, were used for systematic studies: V1 covered the front frame of WC1, and V2 and V3 covered the frame of WC3 and the front flange of the NaI(Tl) crystal enclosure, respectively. Detector parameters are given in Table 1.

3. Design and construction

The experimental apparatus was constructed in modules (PIENU-I and PIENU-II) for simplification of installation and servicing. PIENU-I consisted of V1, WC1, WC2, B1, B2, S1, S2, B3, S3 and T1, while PIENU-II included WC3, T2, V2, V3, NaI(Tl) and Csl.

PIENU-I was attached to the end of the beam pipe and could be divided into three sub-assemblies (V1+WC1+WC2, B1+B2+S1+S2 and B3+S3+T1). The PIENU-II detector assembly was supported on a cart. During normal running conditions the cart rested on rails which were aligned with the beamline and PIENU-I in the X–Y plane. Modularity allowed a number of supplemental measurements to be performed aimed at evaluating systematic effects during data taking. One of the measurements was determination of the response of the NaI(Tl) and Csl crystal array

⁶ The M13 beamline at TRIUMF was modified in order to reduce the positron contamination in the beam.

⁷ A right-handed coordinate system is used with the origin at the center of the target counter. The Z-axis points in the beam direction, and the Y-axis points upwards.

⁸ Distance from the center of B3 to the central plane of WC3.

⁵ Acceptance was defined by two plastic scintillator counters located downstream of the pion stopping target.

Table 1
PIENU detector parameters.

Plastic scintillator counters					
Trigger counters	B1	B2	B3	T1	T2
Size in X (Inner radius)	100 mm	45 mm	70 mm	80 mm	(0) mm
Size in Y (Outer radius)	100 mm	45 mm	70 mm	80 mm	(171.45) mm
Size in Z	6.604 mm	3.07 mm	8.05 mm	3.04 mm	6.6 mm
Z position	−39.03 mm	−30.02 mm	0 mm	19.92 mm	72.18 mm
Photomultiplier model/	H3178-51	83112-511	XP2262B	83112-511	H3165-10
Manufacturer	Hamamatsu	Burle	Photonis	Burle	Hamamatsu
Photocathode diameter	34 mm	22 mm	44 mm	22 mm	10 mm
Veto counters			V1	V2	V3
Inner radius			40 mm	107.95 mm	177.8 mm
Outer radius			52 mm	150.65 mm	241.3 mm
Size in Z			3.175 mm	6.35 mm	6.35 mm
Photomultiplier model/			H3164-10		H3165-10
Photomultiplier manufacturer			Hamamatsu		Hamamatsu
Photomultiplier Photocathode diameter			8 mm		10 mm
Tracking detectors					
Multi-wire proportional chambers			WC1	WC2	WC3
Wire spacing				0.8 mm	2.4 mm
Number of planes/wires/readout channels				3/120/40	3/96/48
Active area diameter				96.0 mm	230.4 mm
Cathode to anode spacing				1.6 mm	2.0 mm
Wire diameter				15 μ m	
Wire orientation				0°, +120°, −120°	
Silicon strip detector pair (X and Y oriented strips)					S1/S2/S3
Active area					61 × 61 mm ²
Silicon strip pitch					80 μ m
Effective pitch after binding 4 strips					320 μ m
Number of planes/readout channels per plane					2/48
Thickness (size in Z)					0.285 mm
Separation between X and Y strip detectors					12 mm
Electromagnetic calorimeter					
Crystal				Nal(Tl)	CsI
Number used				1	97
Energy resolution (FWHM) at 70 MeV				2.2%	~10%
Thickness (size in Z)				480 mm	250 mm
Outer radius				480 mm	–
Approximate width × height for pentagon shaped CsI crystals				–	90 × 80 mm ²
Number of PMTs per crystal				19	1
Hamamatsu PMT model (central PMT for Nal(Tl) was R1911-07)				R1911	R5543
Photomultiplier photocathode diameter					76.2 mm

to a beam of 70 MeV/c incident positrons at various positions and angles of entrance as described in Section 5.3. This measurement was made possible by leaving only the first sub-assembly of PIENU-I in place, containing V1+WC1+WC2, which detected the incoming beam, and removing the rails in order to allow the PIENU-II assembly to be moved freely within the experimental area.

In 2010, the experimental area was enclosed in a temperature-controlled tent in order to make temperature-related changes in detector's performance negligible. The temperature inside the tent was kept at 20 ± 0.5 °C.

4. Scintillation counters

The plastic scintillators were fabricated from Bicron BC-408 (polyvinyltoluene) scintillator [11] chosen for its high light-output, fast rise (0.9 ns), and short decay (2.1 ns) times. The B1 beam scintillator was large enough to fully cover the aperture of the

multiwire chamber package WC1 and WC2. The B2 scintillator, which was smaller than the B3 scintillator, ensured that the particles going through B2 would hit B3.⁹ T1, located downstream of B3, defined the positron timing. Due to space restrictions and their circular shape, T2 and the veto scintillators (V1–V3) were read out with 1 mm diameter wave-length-shifting (WLS) fibers (Kuraray Y-11) embedded in grooves (1.1 × 1.1 mm² in cross-section) machined on the scintillator surfaces; groove spacing was 10 mm, 3 mm, 10 mm and 11 mm for T2, V1, V2 and V3¹⁰ counters respectively.

Collection of the scintillation light for all the rectangular-shaped scintillators was done with adiabatic light guides which

⁹ The rectangular-shaped B3 and T1 counters were rotated by 45° around the beam axis due to spatial limitations of the mechanical assembly which supported the scintillator along with their respective light guides, photo multiplier tubes (PMTs), and a number of other subdetectors (WC1, WC2, S1, S2, S3).

¹⁰ T2 had linear parallel grooves traversing the counter's surface, while annular veto counters V1, V2 and V3 had circular grooves.

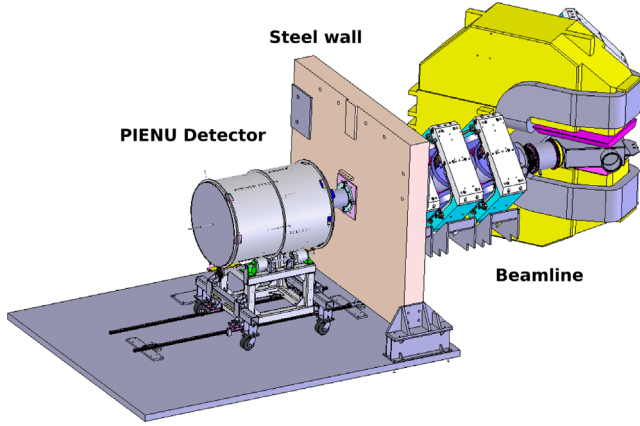


Fig. 2. Computer generated rendering of the PIENU detector and the steel wall used as passive shielding at the end of the M13 beamline.

were cut from UV transparent acrylic sheets and polished. It was important to have a uniform light collection efficiency in order to maximize energy resolution. A schematic of the four-way readout configuration is shown in Fig. 3. Simulations of the optical transport with Detect2000 [12] were used to predict the uniformity of the light collection in this configuration, and were later confirmed with measurements. For example, a variation of $< 1.2\%$ was observed in the visible energy deposited by beam muons in B1 over the counter's surface.

Each scintillator was read out with four photo-multiplier tubes (PMTs), except for V1, V2 and V3 which were each read out with a single PMT. PMTs were selected by photocathode size and ability to match either the 425 nm wavelength of the maximum emission of the Bicron-408 or the 476 nm wavelength of the emission peak of the WLS fibers. Information on the scintillator size and PMTs used is listed in Table 1. All plastic scintillator PMTs were read out with 500 MHz ADCs (see Section 7.2).

T2 was the largest scintillator read out with WLS fibers, having 33 parallel grooves machined on the downstream side. Near the edge of the counter, the grooves were made gradually deeper so that the WLS fibers lying in the grooves could exit perpendicular to the counter's surface with minimum transition space and point upstream where they could be bundled and read out by PMTs (see Fig. 4 for schematic of the T2 grooves). The minimum radius of the groove curvature at the edges of T2 was 19.5 mm. Fibers were thermally pre-bent to reduce stress. T2 fibers were read out on both ends, and bundled into two groups (1–16 and 17–33). As a result, T2 was read out using four PMTs. It had a time resolution of $\sigma_t = 1.4$ ns for minimum ionizing particles when measured against T1 (see Fig. 5) and its efficiency for positrons was measured to be greater than 99.7% within the acceptance region.

The most critical scintillation counter, B3, had an energy resolution of 5% r.m.s. ($T_{\text{visible}} = 3.22 \pm 0.16$ MeV) for 4.1 MeV μ^+ from $\pi^+ \rightarrow \mu^+ \nu_\mu$ decay (see Fig. 6). The time difference between T1 and B1 was used to determine the decay time with a resolution of $\sigma_t = 138$ ps for beam positrons. Both T1 and B1 times were determined from fits of 500 MHz-sampling-frequency waveforms.

5. Calorimeter

The purpose of the PIENU calorimeter system was to detect decay positrons and photons from the $\pi^+ \rightarrow e^+ \nu_e$ and $\pi^+ \rightarrow e^+ \nu_e \gamma$ decays as well as from the $\mu^+ \rightarrow e^+ \nu_e \bar{\nu}_\mu$ and $\mu^+ \rightarrow e^+ \nu_e \bar{\nu}_\mu \gamma$ following the decay $\pi^+ \rightarrow \mu^+ \nu_\mu$. It was composed of a large monolithic NaI(Tl) crystal surrounded by 97 pure CsI crystals.

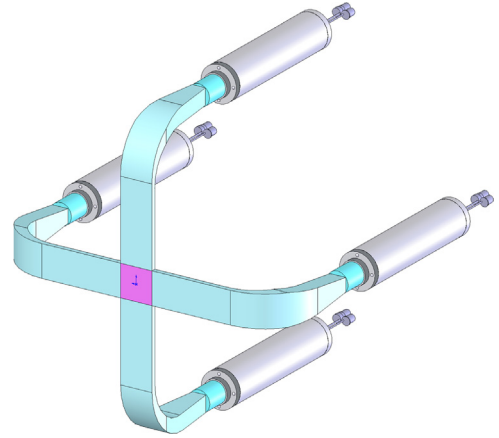


Fig. 3. Schematic view of the B1, B2, B3 and T1 scintillator readout. Light guides were bent adiabatically and coupled to PMTs through acrylic cylinders.

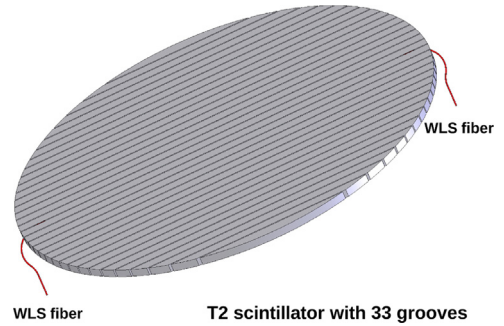


Fig. 4. Schematic drawing of the T2 scintillator. 33 parallel grooves (1.1×1.1 mm²) machined on the surface of the counter were made deeper towards the edge to allow the WLS fibers to exit perpendicular to the counter's surface (see text for details). One such readout WLS fiber is shown for illustration.

Scintillation light collection was realized through directly coupled PMTs.

5.1. NaI(Tl) crystal

The main calorimeter element was a single crystal of thallium-doped NaI on-loan from Brookhaven National Laboratory [9]. The crystal was enclosed in a 3 mm thick aluminum enclosure which had nineteen 76.2 mm diameter circular quartz windows at the rear end. The aluminum front face of the NaI(Tl) was 0.5 mm thick. Each window was viewed by a 76.2 mm diameter Hamamatsu R1911 PMT (with the exception of the central PMT R1911-07) surrounded by a μ -metal shield.

The surface of the crystal was covered with reflective material. An optical simulation was performed using Detect2000 [12] to study the dependence of the energy deposited in the crystal on the entrance location of the particle. Light emitted by the crystal was uniformly reflected,¹¹ and thus a similar amount of light was seen by individual PMTs independent of the entrance position of the ionizing particle on the front face of the NaI(Tl) crystal. This was confirmed within 2% by bench tests using 511 KeV and 1274 KeV γ rays from a ²²Na radioactive source. The calibration of the NaI(Tl) crystal was done with 75 MeV/c beam positrons using a dedicated trigger.

¹¹ For the simulation both specular and diffuse reflectors were modeled, with the reflection coefficient varying between 0.95 and 0.99 and a refractive index of 1.85 was assumed for the NaI(Tl) crystal.

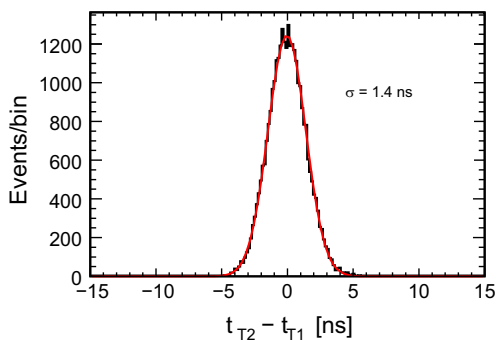


Fig. 5. The observed time difference between T2 and T1. The T1 time is determined by fitting a waveform, while the T2 time is defined as the time of the earliest pulse found within the waveform. Due to WLS fiber readout of T2 several pulses could be seen for one particle. Histogram is data, and the smooth line is a Gaussian fit.

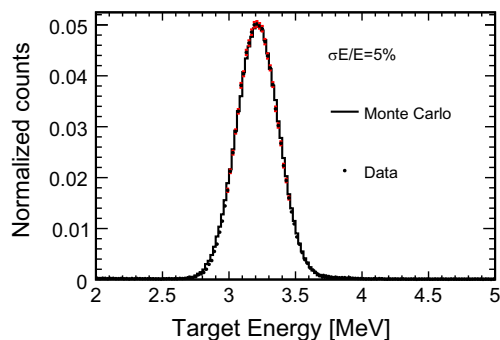


Fig. 6. Visible energy deposited in B3 by a μ^+ with a kinetic energy of 4.1 MeV from $\pi^+ \rightarrow \mu^+ \nu_\mu$ decay. The data is represented by points, and a Monte Carlo simulation by the histogram. The mean visible energy is approximately 3.2 MeV due to saturation of scintillation light.

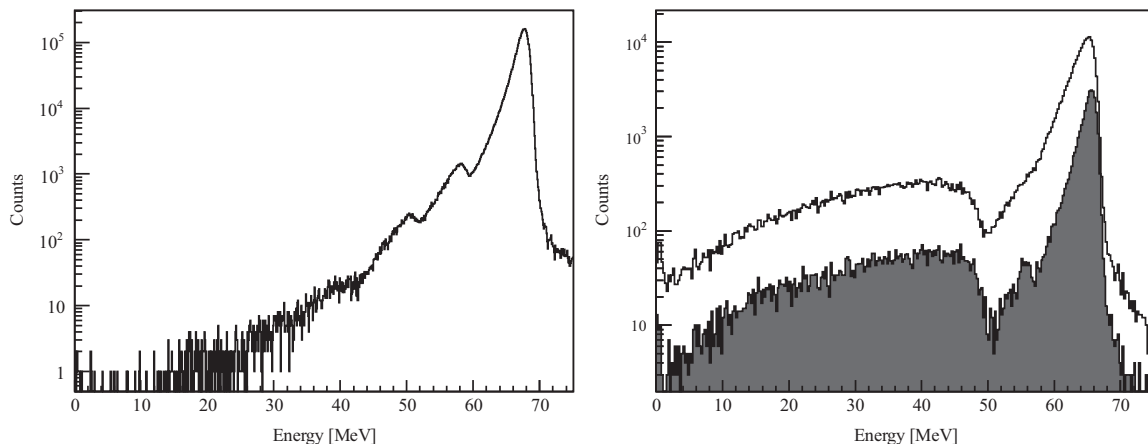


Fig. 7. *Left:* Response of the NaI(Tl) crystal to a positron beam of momentum 70 MeV/c. Below the full energy peak, the additional low energy peak structures are due to photoabsorption followed by neutron escape from the crystal [16]. *Right:* $\pi^+ \rightarrow e^+ \nu_e$ decay spectrum with additional cuts for suppressing the $\pi^+ \rightarrow \mu^+ \nu_\mu$ decays, which can be seen in the energy spectrum up to approximately 50 MeV. The first structure due to photoabsorption in the crystal becomes visible to the left of the main peak (from the $\pi^+ \rightarrow e^+ \nu_e$ decay positron at around 65 MeV) as one restricts the acceptance. The shaded histogram represents a tighter-than-nominal 40 mm radial acceptance cut and the unfilled histogram represents the nominal acceptance cut of 60 mm.

5.2. CsI crystal array

Each crystal within the CsI array was 25 cm (13.5 radiation lengths) long and had pentagonal shape, with an average width of 9 cm and a height of 8 cm (4.5 radiation lengths). The crystals were arranged to form two upstream and two downstream concentric layers around the NaI(Tl). Each concentric layer of crystals was supported by a 2 mm thick stainless steel cylinders with a 2-mm thick fin separating and supporting every 3–5 crystals from its neighbors (6 fins per layer). The resulting array of CsI crystals was 50 cm long and 16 cm (9 radiation lengths) thick in the radial direction. The CsI array was continuously flushed with nitrogen gas to keep the humidity level low. Each crystal was read out by a fine-mesh 76.2 mm diameter Hamamatsu R5543 PMT [13]¹². The pure CsI pulse shape has two components: fast and slow with 30 ns and 680 ns decay times respectively. The fast component constitutes about 20% of the total pulse. In order to suppress the slow component, a UV-transmitting optical filter was present in front of each PMT. Each crystal had a $\text{YAlO}_3:\text{Ce}^{245}\text{Am}$ source [15] attached to its front face to monitor the

crystal's light output and the PMT's gain. The source emits light at a frequency of 50 Hz with similar wavelength and pulse width as the CsI scintillation light with an equivalent energy deposit of 10 MeV. Each crystal was also connected via a quartz fiber to the output of a Xe lamp whose flash was triggered at 2 Hz during data taking. This Xe lamp system was implemented to monitor CsI PMT's gains. Seven reference PMTs of the same type as the ones used for the calorimeter were enclosed in an incubator maintained at a constant temperature of 24.0 °C. The Xe lamp was enclosed in an identical incubator at the same temperature. The Xe-lamp was connected to the reference PMTs through the same system as the CsI crystals so that any changes in the Xe-lamp output could be tracked by the reference PMTs.¹³

The energy calibration of the CsI array was performed with cosmic rays. A dedicated trigger, based on coincidence of the two concentric CsI rings, provided a sample of cosmic ray data. The energy peak due to minimum ionizing muons going through the crystals was compared with a detailed Monte Carlo (MC) simulation of the system to obtain the energy calibration.

¹² The components of the magnetic background in the experimental area have been measured to be < 2 Gauss at the location of the detector, well within the operational specifications of these fine-meshed PMTs. Before being brought to TRIUMF, the crystals and their PMTs were used as endcap photon-veto detector in the E949 experiment at BNL [14]

¹³ The Xe lamp system was found to be stable to less than 1% level and was used for monitoring. Since the whole experimental apparatus was enclosed in the temperature controlled tent, no temperature-dependent variations in the PMT gains were observed, while the PMT gain degradation over time was on the order of $\approx 1\%$ per year.

5.3. Performance

Nal(Tℓ): The response of the *Nal(Tℓ)* crystal was investigated by reconfiguring the detector to include PIENU-II and only the first sub-assembly of PIENU-I (V1, WC1, and WC2).

The response of the crystal to a 70 MeV/c positron beam entering its front face at the center is shown in Fig. 7(left). The high energy peak corresponds to the full energy of the beam positrons. After deconvoluting the beam momentum width of 0.5%, the resolution at 70 MeV/c was 2.2% (FWHM). Below the beam energy, additional structures are visible [16] due to nuclear photoabsorption and subsequent neutron escape. In this process, one or more photons in the shower initiated by the positron are absorbed by iodine and neutrons emitted after the absorption escape the crystal reducing the measured energy by the neutron binding energy of approximately 8 MeV. Structures corresponding to up to three escaping neutrons can be seen in Fig. 7(left). This mechanism was consistent with a MC simulation of the crystal response including electromagnetic and hadronic interactions [16].

Photonuclear effects are also present when measuring the $\pi^+ \rightarrow e^+ \nu_e$ decay positrons. An energy spectrum of the $\pi^+ \rightarrow e^+ \nu_e$ decay positrons with a small (< 15%) contamination of positrons from the $\pi \rightarrow \mu \rightarrow e$ decay chains is shown in Fig. 7(right), where the presence of a structure due to one-neutron escape below the main peak (see also [7]) is evident.

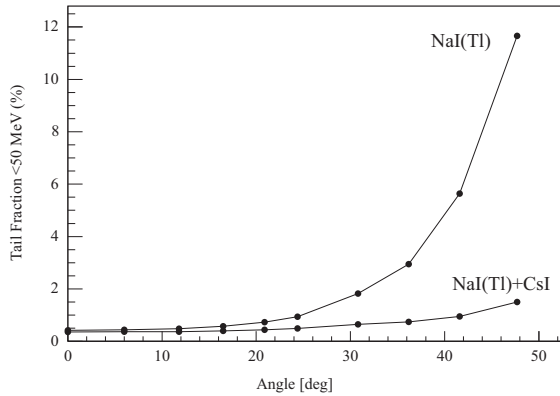


Fig. 8. Fraction of events below 50 MeV for the *Nal(Tℓ)* crystal alone and the *Nal(Tℓ)* plus CsI combination as a function of the angle between the beam and the calorimeter horizontal axis. Error bars are too small to be visible.

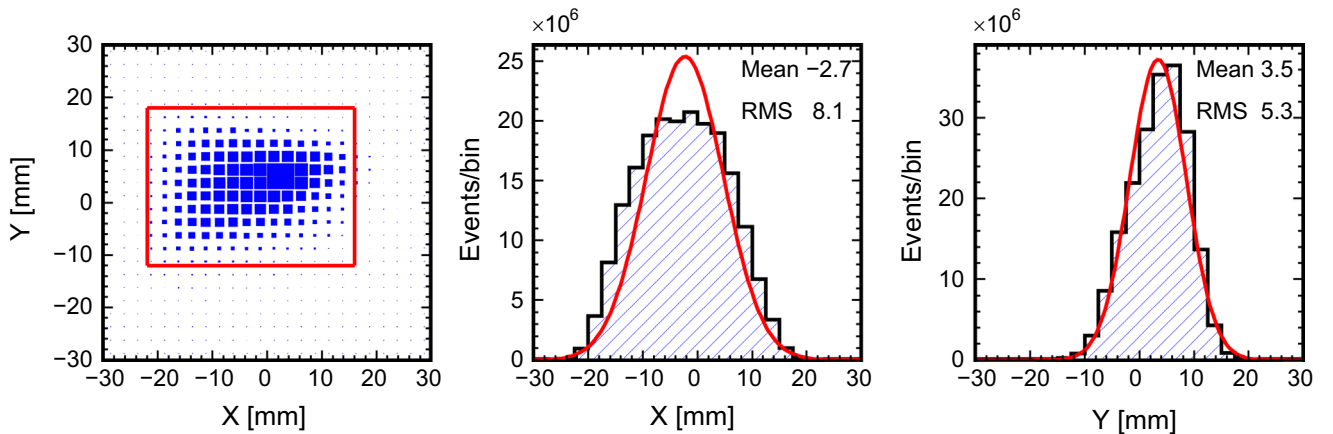


Fig. 9. Beam profile plots. Scatter plot (*Y* vs *X*) of the beam profile at the center of the WC1, the red box indicates the typical boundaries of the incoming particle selection cut (left plot). *X* and *Y* profiles of the beam at the center of WC1 (center and right plots, respectively). *X* and *Y* coordinates are determined by reconstructing the incoming particle's track using WC1 and WC2. (For interpretation of the references to color in this figure caption, the reader is referred to the web version of this paper.)

CsI array: The purpose of the CsI array was the collection of the electromagnetic shower leakage from the main *Nal(Tℓ)* calorimeter. A critical part of the PIENU experiment was the reduction and measurement of the low energy tail from the $\pi^+ \rightarrow e^+ \nu_e$ decay to reduce systematic uncertainties in the correction for events buried under the $\pi \rightarrow \mu \rightarrow e$ decay chain energy distribution. During the measurement of the calorimeter response a positron beam was used to investigate the fraction of the low energy tail as a function of the angle between the beam and the *Nal(Tℓ)* crystal face. The crystal face was rotated to 10 different angles (up to 48°) with respect to the beam. The results are shown in Fig. 8 where the fraction of events below 50 MeV (tail fraction) are reported as a function of the angle. When only the energy of the *Nal(Tℓ)* crystal is considered, the low energy tail fraction reaches 12% for the highest angle, while if the CsI energy is added, the fraction never exceeds 2% over the whole angular range.

6. Tracking devices

The beam wire chambers WC1 and WC2 were used to track the incoming pions (see Fig. 9). Together with the two *X*-*Y* planes of silicon strip detectors (S1 and S2) they could detect pion decay-in-flight events upstream of the target (see Section 6.3). The downstream trackers (S3 and WC3) were used to track the decay positrons after the target. The reconstructed track's position at the center plane of WC3 was used to define the acceptance of the positrons at the entrance of the calorimeters. Upstream (WC1, WC2, S1, and S2) and downstream (S3 and WC3) tracker information was also used to reconstruct the position of the pion's decay vertex in the target. WC3 was also used to detect pile-up events which were not detected by the upstream trackers or S3 which had smaller recording time windows (see Section 7.2).

6.1. Multiwire proportional chambers

Each wire chamber (WC1, WC2 and WC3) consisted of three wire planes which were rotated by an angle of 120° with respect to each other. The chambers were filled with a tetrafluoromethane (CF₄)-isobutane (C₄H₁₀) mixture (80%-20%) at atmospheric pressure. Each wire plane of WC1 and WC2 had 120 wires (0.8 mm in pitch) grouped by three. Each group was connected to a read-out pad. The number of read-out channels was 40 per plane. The active diameters of WC1 and WC2 were 9.6 cm. The chamber WC3, mounted on the flange of the *Nal(Tℓ)* crystal enclosure, measured the position of the decay positrons at the entrance of the

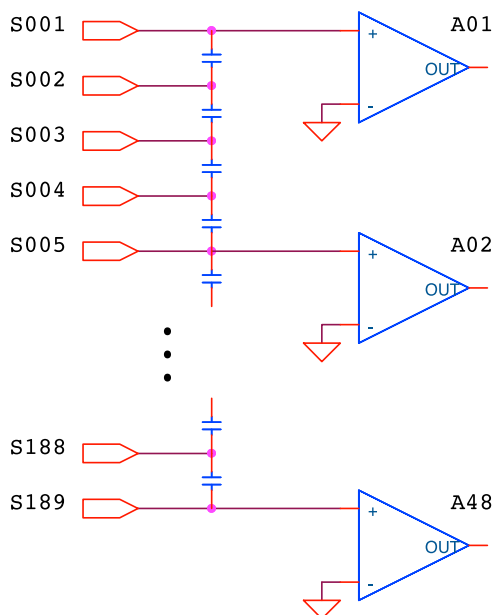


Fig. 10. Schematic drawing of the silicon strip detector readout scheme.

calorimeter, and defined the acceptance region. Each plane had 96 wires with a pitch of 2.4 mm. The wires were grouped in pairs which reduced the number of channels to 48. The active diameter of WC3 was 23 cm. The efficiency of every plane was measured to be $> 99\%$ for beam positrons.

6.2. Silicon strip detectors

Each set of silicon strip detectors (S1, S2, and S3) consisted of two identical hybrids fixed back to back with perpendicular orientation of strips (to measure X and Y coordinates). Each silicon detector had an active volume of $61 \text{ mm} \times 61 \text{ mm} \times 285 \mu\text{m}$. The Si sensor was a single sided AC-coupled micro-strip detector. In the original design [17], strips had a pitch of $80 \mu\text{m}$ but since the required resolution for the PIENU experiment was of the order of $300 \mu\text{m}$, four strips were bound to one read-out line. For further reduction of the number of readout channels, the readout lines were interconnected with capacitors and only every fourth line was read out by an amplifier as shown in Fig. 10. Forty eight channels per silicon plane (288 channels in total) were read out. The capacitive network formed a charge division line where the reconstruction of the ionization amplitude and position was made by weighting of two or three channels that typically had a signal due to a charged particle traversing the sub-detector. The final position resolution (rms) provided by each silicon plane was $95 \mu\text{m}$ if at least two readout channels had a signal and $370 \mu\text{m}$ when the signal was recorded in only one readout channel. In order to reduce the data size, a hardware threshold was set to suppress channels with no hits. In S1 and S2, the thresholds were optimized for the detection of pions while the S3 thresholds were set lower to ensure that the detection efficiency for decay positrons in at least one plane (X or Y) was higher than 99%.

6.3. Performance

This compact assembly of tracking devices was designed to minimize the major source of background for the measurement of $\pi^+ \rightarrow e^+ \nu_e$ decay due to decay of pions in flight. About 3.6% of the

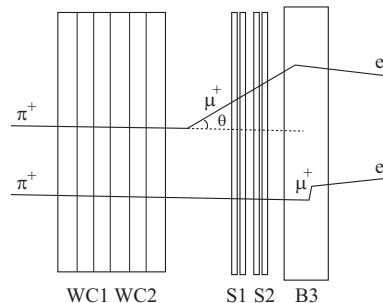


Fig. 11. Schematic representation of pion-DIF and pion-decay at rest (PDAR) event. Events with decay in flight show an inconsistency between the directions of the track segments reconstructed in WC1 and WC2, and S1 and S2, while track directions are consistent for decays at rest.

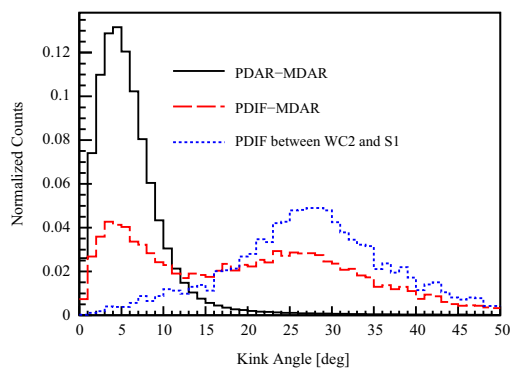


Fig. 12. Kink angle measured by WC1–WC2 and S1–S2 tracking devices from MC. About half of the pion-DIF events happen after S1 and cannot be distinguished from pion-DAR (PDAR) or muon-DAR (MDAR) events. DAR stands for decay-at-rest.

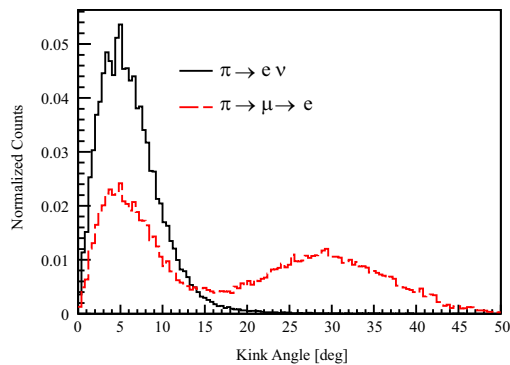


Fig. 13. Kink angle for $\pi^+ \rightarrow e^+ \nu_e$ ($T_{\text{Nat}(T\tau)} > 55 \text{ MeV}$) and $\pi^+ \rightarrow \mu^+ \rightarrow e^+$ ($T_{\text{Nat}(T\tau)} < 30 \text{ MeV}$) data events. The presence of pion-DIF events in the $\pi^+ \rightarrow \mu^+ \rightarrow e^+$ sample can be clearly seen at angles $> 15^\circ$.

pions entering the PIENU detector¹⁴ decay in flight upstream or inside the target. This type of decay, labeled pion-DIF for pion decay-in-flight, will have a low energy deposit in the target and can therefore mimic the energy deposition of a $\pi^+ \rightarrow e^+ \nu_e$ decay. About half of those pion-DIF events happen upstream of the target, between WC2 and S1, and can be identified by the tracking detectors as illustrated in Fig. 11.

The distributions of the angle (kink angle) between the track detected by WC1 and WC2 and the track detected by S1 and S2 for different decay types are shown in Fig. 12 for MC and in Fig. 13 for

¹⁴ This result is obtained from the Geant4 simulation. A pion is denoted as entering the detector if it enters the first detector element WC1.

data. Pion-DIF events between WC2 and S1 can be distinguished due to their higher kink angle.

7. Trigger and data acquisition system

7.1. $\pi^+ \rightarrow e^+ \nu_e$ run trigger

Pions and a fraction of beam muons and positrons (used for the calibration of some detectors) were selected by the trigger using energy deposit information in B1. Definition of a beam particle was done by requiring the coincidence of the beam counters B1, B2, and B3. A coincidence of T1 and T2 counters defined the decay-positron signal. A coincidence of beam pion and decay positron signals (PIE) within a time window of -300 ns to 500 ns was the basis of the main trigger logic. Since $\pi^+ \rightarrow \mu^+ \nu_\mu$ decays happen much more often than $\pi^+ \rightarrow e^+ \nu_e$ decays, a *Prescale* trigger precisely selected only 1/16 of PIE events. Meanwhile, the

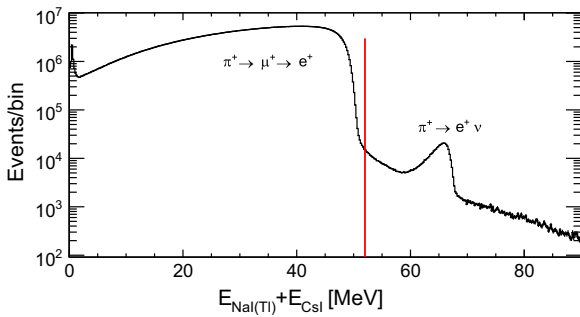


Fig. 14. Measured energy in NaI(Tl) and CsI array for a portion of collected data. The vertical line denotes separation of collected events into low-energy (dominated by $\pi^+ \rightarrow \mu^+ \nu_\mu$ decays) and high-energy (dominated by $\pi^+ \rightarrow e^+ \nu_e$ decays and pile-up).

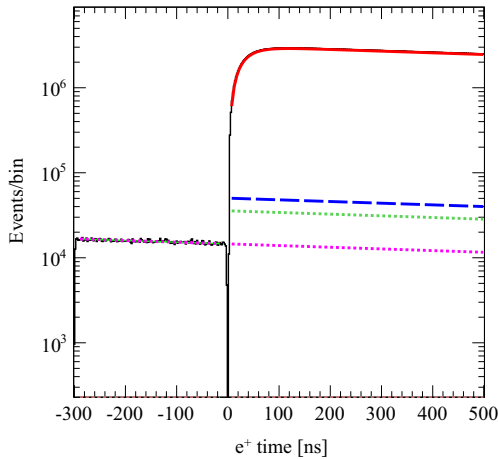


Fig. 15. Time spectrum defined by the time difference between T1 and B1 hits for low-energy events. Zero time corresponds to the time of the pion stop. The solid (red) line represents the fit function describing the $\pi^+ \rightarrow \mu^+ \rightarrow e^+$ decay chain, the dashed (blue) line represents the sum of backgrounds, represented by two dotted lines which correspond to muon decays and pion decays in flight. (For interpretation of the references to color in this figure caption, the reader is referred to the web version of this paper.)

$\pi^+ \rightarrow e^+ \nu_e$ events were enhanced by the *Early* and *HE* (High Energy) triggers. The *Early* trigger selected decays which happened between 2 ns and 40 ns (excluding prompt events) after the pion stop. Due to the 26 ns pion lifetime, more than 70% of the $\pi^+ \rightarrow e^+ \nu_e$ events happen within this time range. The *HE* trigger

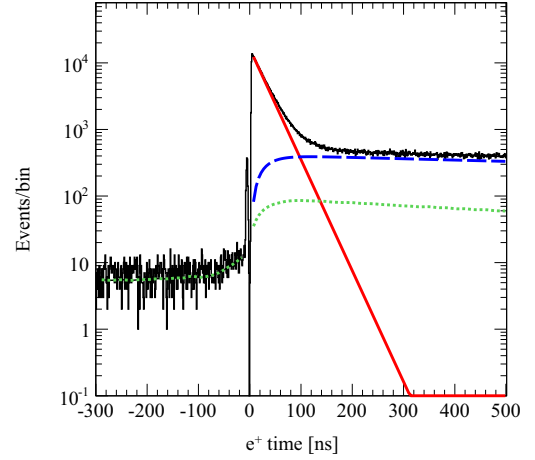


Fig. 16. Time spectrum defined by the time difference between T1 and B1 hits for high-energy events. Zero time corresponds to the time of the pion stop. The solid (red) line represents the fit function describing the $\pi^+ \rightarrow e^+ \nu_e$ time spectrum, the dashed (blue) line represents the $\pi^+ \rightarrow \mu^+ \rightarrow e^+$ decay chain events which due to pulse pile up ended up in the high energy spectrum, and the dashed line represents the sum of the remaining background mechanisms like charged pileup and radiative decays. (For interpretation of the references to color in this figure caption, the reader is referred to the web version of this paper.)

Table 2
Trigger rates.

Trigger	Rate (Hz)
Pion stop in target	5×10^4
<i>Physics triggers</i>	
Early trigger	160
HE trigger	170
Prescale trigger	240
<i>Other triggers</i>	
Cosmics trigger	15
Beam Positron trigger	5
Xe lamp trigger	2
Total Triggers	600

was based on a VME-module which summed the energy deposited in the calorimeters in real time. The trigger signal was produced by this module for events which had a high energy deposited in the NaI(Tl) and CsI spectrometers. The energy threshold was set 4 MeV below the highest energy of the positron from the $\pi^+ \rightarrow \mu^+ \rightarrow e^+$ decay chain. Almost all the $\pi^+ \rightarrow e^+ \nu_e$ events (with the exclusion of the tail events which extend below the e^+ energy spectrum from the $\pi^+ \rightarrow \mu^+ \rightarrow e^+$ decay chain) were selected by this trigger. Those three triggers constituted the “physics triggers”. Additional triggers were used for data quality checks and calibration purposes. The *Xe-lamp* trigger provided flashes twice a second to all CsI crystals. Both these triggers (*Xe-lamp* and *Cosmic*) were intended for CsI calibration and monitoring. Finally, the *Beam positron* trigger triggered on one of every 32 beam positrons to calibrate the NaI(Tl) crystal. During a run, all 6 triggers were used and several of them could be satisfied at the same time. The rates of the various triggers are shown in Table 2. The trigger signal issued by any of the six triggers was then latched by the pion (t_{π^+}) and the positron (t_{e^+}) timings in order to reference the gate of the data acquisition modules to the incoming and decay particles, respectively. These latched signals triggered the data acquisition.

T_{e^+} was used to trigger the data acquisition by the VME modules (VF48 and VT48, which are described below) while T_{π^+} triggered the COPPER data acquisition, described below.

7.2. Data acquisition system

COPPER: This 500-MHz-sampling-frequency Flash ADC (FADC) system was based on the COPPER (Common Pipelined Platform for Electronics Readout) platform. The detailed characteristics of the COPPER system have been described in Refs. [18,19]. The PIENU experiment was equipped with four COPPER boards¹⁵ to digitize the signals coming from the 23 PMTs reading out the plastic scintillators, analog sum of NaI($T\ell$) PMTs, and partial analog sums of CsI array PMTs. The time window of the signals recorded by COPPER covered 7.74 μ s (1.35 μ s after and 6.39 μ s before the pion stop) to be able to detect pre- and post-pile up particles. The waveforms recorded by COPPER were fitted, on an event-by-event basis, using templates obtained from a spline interpolation of the average PMT pulse shape.

VF48: The VF48 is a 48 channel 60 MHz FADC [20]. It has a resolution of 10 bits and a dynamic range of ± 250 mV. All the NaI ($T\ell$) and the CsI PMT signals as well as all the silicon strip channels were read out by VF48 modules. This made a total of 404 channels (NaI($T\ell$): 19, CsI: 97, silicon strips: 288) read out by 10 VF48 modules). Typically, the VF48 read out 40 samples around the time defined by the decay positron. All VF48 modules were fed with the same 20-MHz clock provided by another VME module. This clock was multiplied internally in the VF48 to reach 60-MHz sampling. Data suppression was implemented in all channels except those reading the NaI($T\ell$) crystal PMTs. Additionally, due to the slow NaI ($T\ell$) response, its waveforms were digitized at a rate of 30 MHz instead of 60 MHz.

VT48: Discriminated signals from the three wire chambers (WC1, WC2, and WC3), all the logic signals issued by the PMT signals after discrimination, and most trigger logic signals were read out by multi-hit time-to-digital converter [21]. This device, based on the AMT-2 chips [22], has a 25-MHz on-board clock which is multiplied to achieve 0.625 ns resolution. All VT48s, however, were fed with an external 25-MHz clock to ensure the synchronization of modules. One board can read out 48 channels for up to 20 μ s. To optimize the dead-time, only two channels were read out for 20 μ s to detect long-lifetime backgrounds originating from the beam while all other channels were read out 4.0 μ s before and after the time defined by the decay positron signal in T1. In total, 11 VT48 modules were used in the experiment.

The PIENU data acquisition system consisted of three VME crates (two VMEs hosted the VF48 and VT48 modules while the third mostly ran slow control modules and modules used by the COPPER system) controlled by VME master modules, and four COPPER boards with a processor on each board. Each processor was running the associated front end programs to transfer the data to a host computer. Collection of the data was done by the MIDAS data acquisition system which incorporates an integrated slow control system with a fast online database and a history system [23]. The MIDAS server computer can be controlled via a web interface. All the information and errors from the DAQ modules were issued on the web page and programs checking the quality of the data online were connected to MIDAS during data taking.

8. Conclusion

The PIENU detector was commissioned in 2009 and was operated during physics and supplemental measurements

including NaI($T\ell$) response measurements until the end of 2012. The branching ratio $R^{e/\mu}$ will be determined from the observed numbers of $\pi^+ \rightarrow e^+ \nu_e$ and $\pi^+ \rightarrow \mu^+ \rightarrow e^+$ events. The summed energy in the NaI($T\ell$) and CsI array for events in the time window -300 to $+500$ ns in relation to the pion stop time is shown in Fig. 14 where the energy spectrum is divided into two regions at 52 MeV: low-energy events dominated by $\pi^+ \rightarrow \mu^+ \rightarrow e^+$ decays, and high-energy events dominated by $\pi^+ \rightarrow e^+ \nu_e$ decays. The time spectra for these two regions shown in Figs. 15 and 16 are used to determine the raw branching ratio taking into account various background components such as pile-up hits from previous muon decays, and pion decays-in-flight. The $R^{e/\mu}$ is then determined after various corrections are made (See Section 1). The excellent performance of the crystal array and tracking array paired with good time resolution achieved in plastic scintillators (B1, T1) were important aspects of the PIENU apparatus ensuring the possibility of a successful measurement of $R^{e/\mu}$ and improved searches for heavy neutrinos [7].

Acknowledgments

We wish to thank P. Amaudruz, R. Bula, S. Chan, M. Constable, C. Lim, N. Khan, R. Kokke, P. Lu, K. Olchanski, R. Openshaw, C. Pearson and R. Poutissou for their contributions to the engineering, installation and commissioning of the detector and DAQ-related work. We are also grateful to Brookhaven National Laboratory for providing the NaI($T\ell$) and CsI crystals. This work was supported by the Natural Science and Engineering Council (NSERC) and the National Research Council of Canada through its contribution to TRIUMF and supported by JSPS KAKENHI Grant numbers 18540274, 21340059, 24224006.

References

- [1] D.I. Britton, et al., *Physical Review Letters* 68 (1992) 3000.
- [2] D.I. Britton, et al., *Physical Review D* 49 (1994) 28.
- [3] G. Czapek, et al., *Physical Review Letters* 70 (1993) 17.
- [4] W.J. Marciano, A. Sirlin, *Physical Review Letters* 71 (1993) 3629.
- [5] V. Cirigliano, I. Rosell, *Journal of High Energy Physics* 0710 (2007) 005.
- [6] D. Bryman, W.J. Marciano, R. Tschirhart, T. Yamanaka, *Annual Review of Nuclear and Particle Science* 61 (2011) 331.
- [7] M. Aoki, et al., *Physical Review D* 84 (2011) 052002.
- [8] A.A. Aguilar-Arevalo, et al., *Nuclear Instruments and Methods in Physics Research Section A* 609 (2009) 102.
- [9] G. Blanpied, et al., *Physical Review Letters* 79 (1997) 4337.
- [10] S. Adler, et al., *Physical Review D* 77 (2008) 052003.
- [11] Bicron BC-408 Specifications Sheet, 1998.
- [12] F. Cayouette, et al., *IEEE Transactions on Nuclear Science NS-49* (2002) 624.
- [13] T. Komatsubara, et al., *Nuclear Instruments and Methods in Physics Research Section A* 404 (1998) 315.
- [14] I.H. Chiang, et al., *IEEE Transactions on Nuclear Science NS-42* (1995) 394.
- [15] M. Kobayashi, et al., *Nuclear Instruments and Methods in Physics Research Section A* 337 (1994) 355.
- [16] A.A. Aguilar-Arevalo, et al., *Nuclear Instruments and Methods in Physics Research Section A* 621 (2010) 188.
- [17] A. Abdesselam, et al., *Nuclear Instruments and Methods in Physics Research Section A* 568 (2006) 642.
- [18] Y. Igarashi, et al., *IEEE Transactions on Nuclear Science NS-52* (2005) 2866.
- [19] K. Yamada, et al., *IEEE Transactions on Nuclear Science NS-54* (2007) 1222.
- [20] J.P. Martin, P.A. Amaudruz, *IEEE Transactions on Nuclear Science NS-53* (2006) 715.
- [21] C. Ohlman, 48-Channel Time-to-Digital (TDC) Module, User's Manual, unpublished.
- [22] Y. Arai, Y. Kurumisawa, T. Emura, Development and a SEU test of a TDC LSI for the ATLAS muon detector, in: KEK-PREPRINT-2001-123, 2001, p. 185.
- [23] S. Ritt, P.A. Amaudruz, The MIDAS Data Acquisition System, URL (<http://http://midas.triumf.ca>).